ACS Energy Letters

Cite This: ACS Energy Lett. 2020, 5, 192−199

http://pubs.acs.org/journal/aelccp

Identifying Electrocatalytic Sites of the Nanoporous Copper−Ruthenium Alloy for Hydrogen Evolution Reaction in Alkaline Electrolyte

Qiuli Wu,[†,#] Min Luo,[‡,#] Jiuhui Han,[§] Wei Peng,[†] Yang Zhao,[†] Dechao Chen,[†] Ming Peng,[†] Ji Liu,[†] Frank M. F. de Groot,[∥] and Yongwen Tan*,[†]

[†]College of Materials Science and Engineering, Hunan University, Changsha, Hunan 410082, China

[‡]Department of Physics, Shanghai Polytechnic University, Shanghai 201209, China

[§]Advanced Institute for Materials Research, Tohoku University, Sendai 980-8577, Japan

[∥]Inorganic Chemistry & Catalysis, Debye Institute for Nanomaterials Science, Utrecht University, Universiteitsweg 99, 3584 CG Utrecht, The Netherlands

Supporting Information

ABSTRACT: Hydrogen production from electrochemical water splitting is a promising route to pursue clean and sustainable energy sources. Here, a three-dimensional nanoporous Cu−Ru alloy is prepared as a high-performance platinum-free catalyst for hydrogen evolution reaction (HER) by a dealloying process. Significantly, the optimized nanoporous alloy $Cu_{53}Ru_{47}$ exhibits remarkable catalytic activity for HER with nearly zero onset overpotential and ultralow Tafel slopes (~30 and ~35 mV dec^{-1}) in both alkaline and neutral electrolytes, achieving a catalytic current density of 10 mA cm^{-2} at low overpotentials of ~15 and ~41 mV, respectively. Operando X-ray absorption spectroscopy experiments, in conjunction with DFT simulations, reveal that the incorporation of Ru atoms into the Cu matrix not only accelerates the reaction step rates of water adsorption and activation but also optimizes the hydrogen bonding energy on Cu and Ru active sites, improving the intrinsic activity for HER.

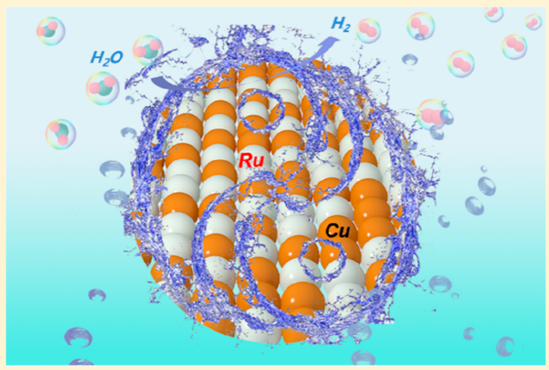

Hydrogen (H_2) generation through electrochemical water splitting is considered as an efficient route to meet the growing demands for renewable and clean energy resources.[1−3] As a critical component of electrochemical water splitting technologies, electrocatalysts determine the energy conversion efficiency of hydrogen evolution reaction (HER), which urgently needs high-efficiency catalysts with low overpotential for large-scale applications.[4,5] Platinum (Pt) is regarded as the most efficient HER catalyst in acidic media, but it shows 2−3 orders of magnitude lower conversion efficiency when operating in basic or neutral media due to its much more sluggish water dissociation capability during the HER process.[6−8] Although nonprecious-metal-based catalysts have been widely explored as enhanced HER catalysts through accelerating the kinetics of water dissociation and hydrogen evolution, including transition metals (such as Fe, Co, Ni, Mo, and W) and their alloys,[9−12] compounds (such as sulfides,[13,14] selenide,[15,16] carbides,[17] phosphides,[18,19] and related hybrids[20]) have turned out to be competitive candidates but still inferior to the Pt-based catalysts in overpotential and durability. Therefore, it is highly desirable to explore novel HER catalysts with better activity than commercial Pt/C in basic and neutral media.

Recently, encouraging progress has been made by alloying transition metals with other noble metals.[11,21] Although the alloying is considered an efficient strategy to enhance the HER performance, a deeper understanding of the origins behind their remarkable catalytic efficiency for alloy electrocatalysts is still ambiguous. Synchrotron radiation-based X-ray absorption spectroscopy (XAS) analysis, together with experimental characterization and theoretical simulation, has gradually been introduced to identify the actual catalytic active sites of the HER. However, due to the difficulty in identifying catalytic

Received: October 30, 2019
Accepted: December 10, 2019
Published: December 10, 2019

DOI: 10.1021/acsenergylett.9b02374
ACS Energy Lett. 2020, 5, 192−199

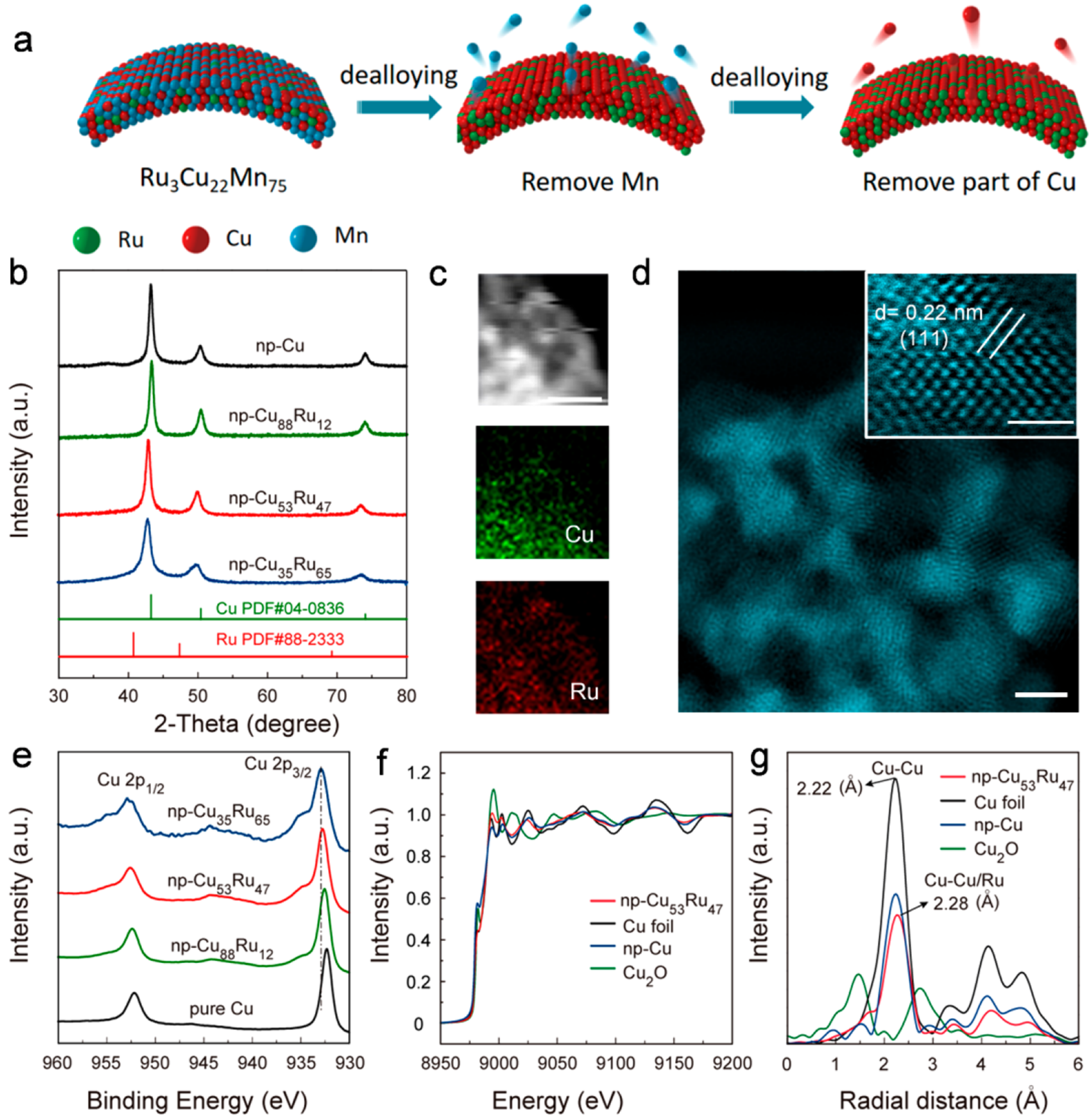

Figure 1. Preparation and characterization of np-$Cu_{100-x}Ru_x$. (a) Schematic illustration of the preparation procedure. (b) XRD patterns of np-Cu, np-$Cu_{88}Ru_{12}$, np-$Cu_{53}Ru_{47}$, and np-$Cu_{35}Ru_{65}$. (c) STEM-EDX elemental mapping of np-$Cu_{53}Ru_{47}$. (d) HAADF-STEM image. Inset: magnified image. (e) Cu 2p core-level XPS spectra recorded on np-$Cu_{88}Cu_{12}$, np-$Cu_{53}Ru_{47}$, np-$Cu_{35}Ru_{65}$, and np-Cu. (f) Normalized XANES at the Cu K-edge of np-$Cu_{53}Ru_{47}$, Cu foil, np-Cu, and Cu_2O. (g) FT k^3-edge weighted c(k)-function of the EXAFS spectra for the Cu K-edge. Scale bars: (c,d) 5 nm, inset of (d): 1 nm.

active sites under realistic operation conditions, it has been challenging to construct and identify new catalysts with better activity and stability than Pt-based catalysts. Herein, we present a new platinum-free nanoporous (np) Cu−Ru alloy as a high-performance electrocatalyst for the HER. As an earth-abundant and low-cost metal, monometallic Cu is known to be poor HER catalysts because their hydrogen binding energy (HBE) values are too weak.[22,23] However, ruthenium is regarded as a promising HER electrocatalyst in alkaline media due to the fast water dissociation process.[24−26] However, the interaction between Ru and H atoms is usually too strong such that making the subsequent hydrogen desorption process becomes more difficult. By alloying Cu with Ru, the incorporation of Ru atoms in the Cu matrix enhances the strength of Cu−H interaction, while it weakens the strong Ru−H interaction to significantly improve the overall HER efficiency in basic or neutral media via accelerating water adsorption/activation and optimizing H adsorption/desorption. Combined with the unique three-dimensional interconnected porous structure, it is beneficial to charge transfer and electrolyte infiltration during the HER process. Significantly, the optimized np-$Cu_{53}Ru_{47}$ exhibits long-term operation stability with nearly zero onset overpotential and ultralow Tafel slopes (∼30 and ∼35 mV dec^{-1}) in both 1.0 M KOH and 1.0 M phosphate buffer solution (PBS) electrolytes, achieving a catalytic current density of 10 mA cm^{-2} at low overpotentials of ∼15 and ∼41 mV, respectively. These impressive HER performances are comparable to the values of state-of-the-art catalyst materials[24,27,28] or even better than them (including the commercial Pt/C catalyst).[2,11,26,29,30]

Nanoporous binary Cu−Ru alloys are prepared through dealloying a single-phase ternary $Ru_3Cu_{22}Mn_{75}$ precursor in $(NH_4)_2SO_4$ solution to remove Mn (Figures S1, S2, and 1a);[31−34] then, the atomic ratio of Cu/Ru in the binary Cu−Ru alloy is further tuned by controlling the corrosion time and is confirmed by energy-dispersive X-ray spectroscopy (EDS)

DOI: 10.1021/acsenergylett.9b02374
ACS Energy Lett. 2020, 5, 192−199

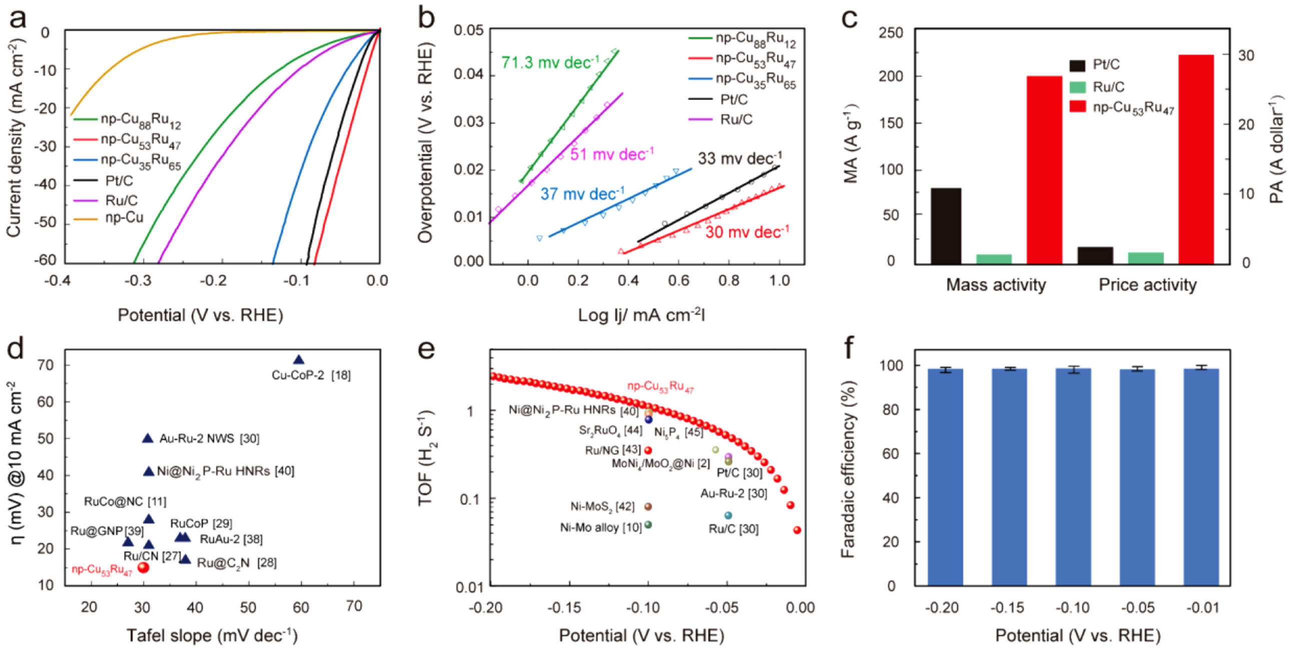

Figure 2. HER activity of nanoporous Cu−Ru alloy electrocatalysts. (a) Polarization curves and (b) Tafel plots of np-$Cu_{88}Ru_{12}$, np-$Cu_{53}Ru_{47}$, and np-$Cu_{35}Ru_{65}$ for HER with *iR* compensation in 1.0 M KOH. (c) Mass activity (MA) and price activity (PA) of Pt/C, Ru/C, and np-$Cu_{53}Ru_{47}$ at the overpotential of η = 50 mV vs RHE. (d) Comparison of both the kinetics (Tafel slope) and activity (the overpotential required to achieve 10 mA cm^{-2}) with references all measured for HER in alkaline electrolyte. (e) TOF values of np-$Cu_{53}Ru_{47}$ (red dot) together with previously reported HER electrocatalysts at −100 mV vs RHE. (f) Faraday efficiency obtained by np-$Cu_{53}Ru_{47}$ in 1.0 M KOH.

and an inductively coupled plasma-optical emission spectrometer (ICP-OES) (Figure S3 and Table S1). X-ray diffraction (XRD) shows the three main peaks of a single-phase face-centered cubic (FCC) structure with the lattice parameters between those of FCC Ru (PDF #88-2333) and FCC Cu (PDF #04-0836) (Figure 1b), indicating the homogeneous formation of the np-$Cu_{100-x}Ru_x$ (x = 12, 47, 65) alloy. We then performed Rietveld refinements of the XRD patterns in order to obtain further information on the structure of the prepared nanoporous alloys. The lattice constant of np-$Cu_{53}Ru_{47}$ is estimated to be 3.692 Å for the FCC phase (Figure S4), whereas those of np-Cu and standard FCC Ru are 3.621 and 3.825 Å (mp-8639). The correlation between the calculated lattice constants and the metal compositions of the nanoporous Cu−Ru is shown in Figure S5. The lattice constants follow Vegard's law well, with small deviations due to the lattice strain caused during the dealloying process.[35] These results indicate the formation of the np-$Cu_{53}Ru_{47}$ solid−solution alloy.[36,37] The energy-dispersive X-ray (EDX) spectroscopy elemental mapping further demonstrates that Ru and Cu atoms are uniformly distributed in the synthesized np-$Cu_{53}Ru_{47}$ alloy (Figure 1c). The color contrast between the bright ligaments and dark pores from high-angle annular dark field-scanning transmission electron microscopy (HAADF-STEM) image indicates the formation of an interpenetrating ultrafine ligament and nanopore structure with a pore size of less than 5 nm (Figure 1d); these results indicate that we successfully synthesized nanoporous binary Cu−Ru alloys with different components through a dealloying process. N_2 adsorption−desorption measurements further verified that np-$Cu_{53}Ru_{47}$ shows a large Brunauer−Emmett−Teller (BET) surface area of 80.21 m^2/g with an average nanopore size of ca. 3.5 nm using the Barrett−Joyner−Halenda (BJH) method (Figure S6). X-ray photoelectron spectroscopy (XPS) was performed to examine the surface chemical state of the Cu−Ru alloys. Figure 1e shows the Cu 2p core-level spectra of np-$Cu_{100-x}Ru_x$. The Cu 2p peaks gradually shift to higher binding energy with increasing Ru content, which is ascribed to the incorporation of Ru atoms into the Cu matrix, resulting in a slight variation of surface electronic structures in the nanoalloys.[21] Meanwhile, the Ru $3d_{5/2}$ peaks of the np-$Cu_{100-x}Ru_x$ alloy show a negative shift compared to that of pure Ru (280.5 eV) (Figure S7),[38] which is ascribed to the efficient electronic interaction between Ru and Cu atoms in the Cu−Ru alloy, leading Ru to bear a negative charge. X-ray absorption spectroscopy (XAS) is performed to further probe the electronic and local structure of the np-$Cu_{53}Ru_{47}$ at the atomic level. Figure 1f,g exhibits Cu K-edge X-ray absorption near-edge structure (XANES) (Figure 1f) and Fourier transform extended X-ray absorption fine structure (FT-EXAFS) (Figure 1g) spectra, together with the np-Cu, Cu foil, and Cu_2O as comparisons. The EXAFS fitting results are described in Figure S8 and Table S8. The Cu K-edge XANES spectra of np-$Cu_{53}Ru_{47}$ shows a much lower leading edge at 8980 eV compared to that of the np-Cu, which suggests a much lower unoccupied density of 4p states at the Fermi level after incorporation of Ru into the Cu matrix (Figure 1f).[39] The corresponding FT-EXAFS spectra in Figure 1g exhibit a prominent peak at ∼2.28 Å, which is different from the Cu−Cu characteristic peak (∼2.22 Å) of pure np-Cu and Cu foil. This result confirms that Cu−Ru bonds could be formed after incorporation of Ru into the Cu lattice. Besides, there may be some defects in the dealloying process because of the undercoordinated surface atoms, as indicated in Figure 1g, which is expected to enhance the catalytic performance of the np-$Cu_{53}Ru_{47}$ alloy. The Ru K-edge XANES of np-$Cu_{53}Ru_{47}$ shows a small shift to lower energy compared to Ru foil, indicating a lower Ru valence state on np-$Cu_{53}Ru_{47}$ (Figure

DOI: 10.1021/acsenergylett.9b02374
ACS Energy Lett. 2020, 5, 192−199

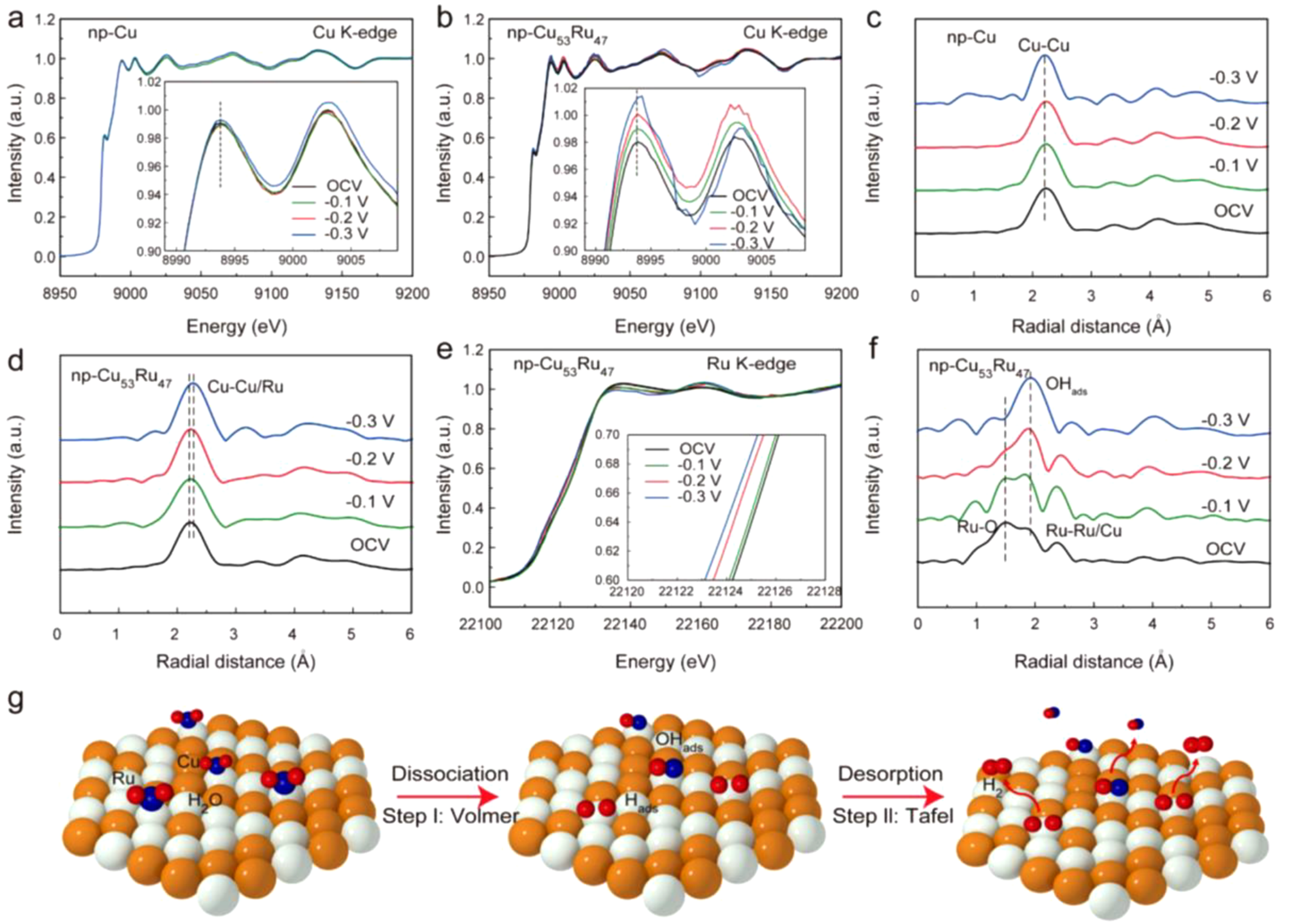

Figure 3. Operando XAS characterization of the np-$Cu_{53}Ru_{47}$ at a series of applied potentials. (a) Operando XANES spectra recorded at the Cu K-edge of np-Cu at different applied voltages from the open-circuit condition to −0.3 V vs RHE during electrocatalytic HER. (Inset) Magnified white line peak XANES region. (b) Operando XANES spectra recorded at the Cu K-edge of np-$Cu_{53}Ru_{47}$ at different applied voltages from the open-circuit condition to −0.3 V vs RHE during electrocatalytic HER (the apparent jitter of curve of the applied voltage at −0.3 V vs RHE is caused by the bubble of hydrogen production). (Inset) magnified white line peak XANES region. (c) Corresponding Fourier transform (FT) XANES spectra of np-Cu. (d) Corresponding FT XANES spectra of np-$Cu_{53}Ru_{47}$. (e) Operando XANES spectra recorded at the Ru K-edge of np-$Cu_{53}Ru_{47}$ at different applied voltages from the open-circuit condition to −0.3 V vs RHE during electrocatalytic HER. (Inset) Magnified pre-edge XANES region. (f) Corresponding FT XANES spectra of np-$Cu_{53}Ru_{47}$. (g) Schematic illustration of the HER mechanism determined by in situ and operando XAS analysis of np-$Cu_{53}Ru_{47}$ in alkaline media.

S9a). The main peak in FT-EXAFS spectra of Ru K-edge displays a different key length from that in Ru foil due to the Ru−Ru/Cu contribution (Figure S9b).[24]

The electrochemical catalytic activities of the np-$Cu_{100-x}Ru_x$ (x = 12, 47, 65) alloys for HER were conducted by a typical three-electrode electrochemical system in Ar-saturated 1.0 M KOH electrolyte. Figure 2a shows the linear sweep voltammetry (LSV) curves with iR correction of np-$Cu_{100-x}Ru_x$ (x = 12, 47, 65), together with commercial Ru/C and Pt/C catalysts as the benchmarks. The onset and operation overpotentials (η) of np-$Cu_{100-x}Ru_x$ show a "decrease−increase" trend with increasing Ru content. The np-$Cu_{53}Ru_{47}$ shows the best HER performance in terms of the extremely low overpotential of −15 mV vs RHE at the electrode current density (j) of −10 mA cm^{-2}, which is 11 and 85 mV lower than those of Pt/C and Ru/C, respectively. Significantly, the np-$Cu_{53}Ru_{47}$ shows a negligible onset overpotential versus RHE in basic solution (Figure S10). The extrapolation from the linear region of the overpotential versus the log j plot (Figure 2b) gives a small Tafel slope of 30 mV per decade (mV dec^{-1}) for np-$Cu_{53}Ru_{47}$, lower than those of Pt/C (33 mV per decade) and Ru/C (51 mV per decade). The electrochemical impedance spectroscopy (EIS) measurements of np-$Cu_{53}Ru_{47}$ further confirm that the incorporation of Ru atoms into the Cu matrix brings about small internal resistance and fast charge transfer behavior (Figure S11), thus realizing rapid HER kinetics. Furthermore, double-layer capacitance (C_{dl}) is identified as an important indicator for the effective electrochemically active surface area, and results reveal a larger C_{dl} of np-$Cu_{53}Ru_{47}$ (59 mF cm^{-2}) compared with that of np-Cu (8.5 mF cm^{-2}) (Figure S12), suggesting more accessible active sites constructed on np-$Cu_{53}Ru_{47}$. The ECSA-normalized LSV curves in Figure S13 are employed to highlight the intrinsic catalytic activity. It is obvious that the ECSA-normalized current density of np-$Cu_{53}Ru_{47}$ is larger than that of np-Cu, implying that the higher HER activity of np-$Cu_{53}Ru_{47}$ results from not only the increased ECSA but also the enhanced intrinsic catalytic activity induced by the incorporation of Ru atoms. Additionally, the mass activity of HER for np-$Cu_{53}Ru_{47}$ at an overpotential of −50 mV vs RHE is 199.59 mA mg^{-1} by normalizing to the Ru loading, which is 2.4 and 18 times greater than those of the commercial Pt/C

DOI: 10.1021/acsenergylett.9b02374
ACS Energy Lett. 2020, 5, 192−199

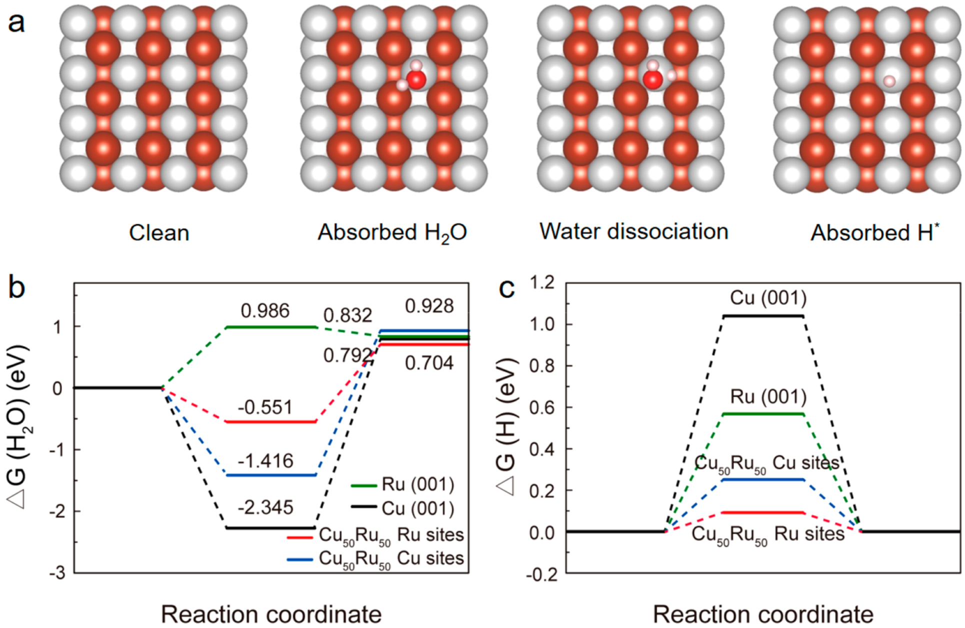

Figure 4. Theoretical calculations of the HER activation energy on Cu−Ru alloy catalysts. (a) Atomic configurations of the water dissociation step on the surface of the $Cu_{50}Ru_{50}$ alloy. Color codes: deep orange and white represent Cu and Ru. Red and light pink represent oxygen and hydrogen atoms in a single water molecule. (b) Calculated adsorption free energy diagram for the Volmer step. (c) Calculated adsorption free energy diagram for the Tafel step.

(10 wt % Pt/C, 81.08 mA mg^{-1}) and Ru/C (10 wt % Ru/C, 10.71 mA mg^{-1}) catalysts, respectively. The price activity of HER for np-$Cu_{53}Ru_{47}$ is also evaluated at an overpotential of −50 mV (Figure 2c and Tables S2 and S3), which is 12 and 18 times greater than those of the commercial Pt/C (2.36 A dollar $^{-1}$) and Ru/C (1.55 A $dollar^{-1}$) catalysts, respectively. These results indicate that the alloying Cu with Ru can maximize the catalytic activity, lowering the cost of HER catalysts. This is further verified by contrast of the Tafel slopes and the overpotentials at a current density of 10 mA cm^{-2} in the basic solution. As shown in Figure 2d, the np-$Cu_{53}Ru_{47}$ exhibits superior HER performance to commercial Pt/C and other available Ru-based HER catalysts in the basic solution (Table S4).[28−30,40,41] The TOF of np-$Cu_{53}Ru_{47}$ at −100 mV vs RHE was calculated to be 1.139 H_2 s^{-1} (Figure 2e), which is better than that of most previously reported catalysts (Table S5).[10,42−45] In addition, the generated H_2 production was analyzed by gas chromatography, which shows that the Faraday efficiency of np-$Cu_{53}Ru_{47}$ is close to 100% under different applied potentials (Figures 2f and S14).

In addition to the basic media, the HER performance of the np-$Cu_{53}Ru_{47}$ is further evaluated in neutral media. As shown in LSV curves (Figure S15a), similar to the HER activities in basic media, the overpotential at 10 mA cm^{-2} of np-$Cu_{53}Ru_{47}$ is only 41 mV in 1.0 M PBS solution, which is not only much smaller than those of commercial Pt/C (50 mV) and Ru/C (128 mV) but also comparable to those of many other reported HER catalysts (Table S6).[46−48] Moreover, the np-$Cu_{53}Ru_{47}$ shows the smallest onset overpotential of ∼2.9 mV vs RHE (Figure S16). The Tafel slope of np-$Cu_{53}Ru_{47}$ (∼35 mV dec^{-1}) is much smaller than the values of Pt/C (∼41 mV dec^{-1}), Ru/C (∼86 mV dec^{-1}), np-$Cu_{35}Ru_{65}$ (∼53 mV dec^{-1}), and np-$Cu_{88}Ru_{12}$ (∼94 mV dec^{-1}) (Figure S15b). Additionally, the durability of the np-$Cu_{53}Ru_{47}$ is evaluated by chronoamperometry in 1.0 M KOH and 1.0 M PBS (Figure S17). The current density of the np-$Cu_{53}Ru_{47}$ alloy shows a negligible change at a continuous applied potential after long-term operation. The HER stability of the np-$Cu_{53}Ru_{47}$ catalyst is also verified by the fact that no detectable change of phase and element valence states of the alloy is observed after long-term operation (Figures S18 and S19). These results unambiguously demonstrate that np-$Cu_{53}Ru_{47}$ has excellent stability.

To elucidate the origins of the high catalytic activities of the nanoporous Cu−Ru alloy, the operando XANES and FT-EXAFS spectra were measured under real HER working conditions to probe the nature activity and local atomic environmental changes of the np-$Cu_{53}Ru_{47}$ alloy with a self-contained unit (Figure S20). During the measurements, the working electrode potential was first increased in steps from the open-circuit voltage (OCV, ∼0.9 V vs RHE) to −0.3 V vs RHE. Figure 3a,b shows the operando Cu K-edge XANES spectra of np-Cu and np-$Cu_{53}Ru_{47}$ alloy at different operating potentials, respectively. As shown in Figure 3a, with an increase of the applied potentials from the OCV to −0.3 V vs RHE, the white line peaks of np-Cu show a negligible change, while those of the np-$Cu_{53}Ru_{47}$ alloy show an obvious shift toward the higher direction intensity (Figure 3b), indicating a change of the local electronic environment of Cu atoms during the HER.[49] The findings are further confirmed by corresponding FT-EXAFS spectra in Figure 3c,d. The extension of the radial distance of the Cu−Cu/Ru shell with the applied bias is observed on the np-$Cu_{53}Ru_{47}$ alloy (Figure 3d), while it is not seen on the np-Cu catalyst (Figure 3c). These results illustrate that the change of electronic structure might promote the interaction between Cu atoms and an intermediate and optimize the adsorption/desorption of H.[38] Moreover, the operando XANES spectra at the Ru K-edge of the np-$Cu_{53}Ru_{47}$ alloy are also recorded in Figure 3e; with an increase of the applied potentials from the OCV to −0.3 V vs RHE, the absorption edge of the Ru K-edge shows an obvious shift toward lower energy, implying a decrease in the Ru valence

DOI: 10.1021/acsenergylett.9b02374
ACS Energy Lett. 2020, 5, 192−199

state of the np-$Cu_{53}Ru_{47}$ alloy during the HER. The result further demonstrates that Cu transfers electrons to Ru during the HER process due to the ligand effects, which can modulate the state of the adsorbed hydrogen intermediate, thereby improving the catalytic activity of the alloy.[50] The results are further verified by FT-EXAFS spectra of the Ru K-edge of the np-$Cu_{53}Ru_{47}$ alloy. As shown in Figure 3f, the scattering of Ru−O at the Ru atoms gradually disappears with an increase of the applied potentials, whereas the intensity of the Ru−OH shell is gradually enhanced during the HER process, which suggests more OH_{ads} adsorbed on Ru atoms in the Volmer reaction of the HER process, thus accelerating the whole HER process in alkaline conditions. Moreover, the decreased intensity and high-R shift observed from the Ru−Ru/Cu shell during HER might be attributed to the interaction of the Ru atom with the OH_{ads}, resulting in a decrease of the coordination number and change of the atomic environment around Ru atoms. On the basis of the operando XAS results of np-$Cu_{53}Ru_{47}$, the HER catalytic reaction is initiated by adsorption of H_2O molecules onto the Ru sites in alkaline electrolyte (Figure 3g) and then undergoes dissociation into intermediate OH_{ads} and H_{ads} on the Ru through the Volmer step. Subsequently, the generated H_{ads} could react with another proton from a neighboring H_2O molecule to generate H_2 (step II shown in Figure 3g). The above results indicate that the incorporation of Ru atoms in a Cu matrix might optimize the electronic structure of the alloy, which not only accelerates H_2O adsorption and dissociation processes but also optimizes adsorption/desorption of H behaviors during the HER.

Density functional theory (DFT) calculations were further carried out to reveal the origins of the superior HER performance on np-$Cu_{53}Ru_{47}$ alloy (Figure 4 and Table S7). The projected density of states (PDOS) results show the orbital hybridization between the Ru 3d orbital and the Cu 3d orbital after the incorporation of Ru atoms into the Cu matrix, which indicates that the alloying could effectively optimize the d-electron domination of Cu and Ru atoms. Significantly, the unoccupied electron density of Cu at the Fermi level increases after the incorporation of Ru atoms into the Cu matrix (Figure S21), while the electron density of Ru decreases, which could be attributed to electron transfer from Ru to Cu after the incorporation of Ru atoms into the Cu matrix. The above observations are in agreement with the XAS measurements (Figure 1g). In general, HER in alkaline or neutral conditions involves a two-step pathway, including adsorption and dissociation of a H_2O molecule, adsorption of H, and desorption of a H_2 molecule from the catalyst surfaces (Figures 4a and S22). The kinetic energy barrier of the prior Volmer step [$\Delta G(H_2O)$] and hydrogen adsorption energy of the Tafel step [($\Delta G(H)$] were calculated based on established electrocatalyst models including the FCC Cu(001), FCC Ru(001), and FCC $Cu_{50}Ru_{50}$(001). As shown in Figure 4b, monometallic Cu has a large water dissociation energy barrier [$\Delta G(H_2O) = -2.345$ eV] for the Volmer step, implying an extremely sluggish Volmer process. In contrast, the $\Delta G(H_2O)$ of the $Cu_{50}Ru_{50}$ alloy at Ru sites decreases to −0.551 eV, even lower than that of monometallic Ru (0.986 eV), indicating that the sluggish Volmer process is obviously accelerated after the incorporation of Ru into the Cu matrix. In addition, the hydrogen adsorption free energy (ΔG_H) in Figure 4c shows a ΔG_H value of 0.092 eV for $Cu_{50}Ru_{50}$ at Ru sites and a ΔG_H value of 0.251 eV for $Cu_{50}Ru_{50}$ at Cu sites, substantively lower than that on monometallic Cu and Ru. These results indicate appropriate H adsorption on Cu and Ru sites of Cu−Ru alloy compared to pure Cu or Ru. Therefore, the incorporation of Ru atoms into the Cu matrix not only accelerates the reaction step rates of water adsorption and activation but also optimizes adsorption−desorption energetics toward H intermediates on Cu and Ru activity sites of the Cu−Ru alloy, improving the HER catalytic activity.

In summary, we have successfully developed novel nanoporous Cu−Ru solid solution alloys whose parent metals are immiscible by rapid solidification combined with a dealloying strategy for high-efficiency HER. Significantly, the optimized np-$Cu_{53}Ru_{47}$ alloy exhibits exceptional performance with a negligible onset overpotential and ultralow Tafel slopes (∼30 and ∼35 mV dec^{-1}) in both 1.0 M KOH and 1.0 M PBS electrolytes, achieving a catalytic current density of 10 mA cm^{-2} at low overpotentials of ∼15 and ∼41 mV, respectively. These excellent HER performances are comparable or even better than that of the state-of-the-art catalysts, including the commercial Pt/C catalyst in terms of both performance and price. Operando X-ray absorption spectroscopy experiments, in conjunction with DFT simulations, demonstrate that the incorporation of Ru atoms into the Cu matrix could effectively optimize the d-electron domination of Cu and Ru atoms and decrease the energy barrier, improving the performance of HER. This work not only successfully synthesizes bimetallic alloys but also sheds light on the realization of inexpensive and efficient systems for energy conversion.

■ ASSOCIATED CONTENT

Supporting Information

The Supporting Information is available free of charge at https://pubs.acs.org/doi/10.1021/acsenergylett.9b02374.

Detailed experimental details and material characterization (PDF)

■ AUTHOR INFORMATION

Corresponding Author

*E-mail: tanyw@hnu.edu.cn.

ORCID

Ming Peng: 0000-0002-8557-1202
Frank M. F. de Groot: 0000-0002-1340-2186
Yongwen Tan: 0000-0003-1486-4048

Author Contributions

#Q.W. and M.L contributed equally to the work.

Notes

The authors declare no competing financial interest.

■ ACKNOWLEDGMENTS

This work was financially supported by the National Natural Science Foundation of China (No. 51771072), the Youth 1000 Talent Program of China, the Fundamental Research Funds for the Central Universities, Hunan University State Key Laboratory of Advanced Design and Manufacturing for Vehicle Body Independent Research Project (No. 71860007), and the State Key Laboratory of Powder Metallurgy, Central South University (No. 621011813).

■ REFERENCES

(1) Chu, S.; Majumdar, A. Opportunities and Challenges for a Sustainable Energy Future. *Nature* **2012**, *488*, 294−303.

(2) Zhang, J.; Wang, T.; Liu, P.; Liao, Z.; Liu, S.; Zhuang, X.; Chen, M.; Zschech, E.; Feng, X. Efficient Hydrogen Production on $MoNi_4$ Electrocatalysts with Fast Water Dissociation Kinetics. *Nat. Commun.* **2017**, *8*, 15437.

(3) Turner, J. A. Sustainable Hydrogen Production. *Science* **2004**, *305*, 972−974.

(4) Xu, K.; Cheng, H.; Lv, H.; Wang, J.; Liu, L.; Liu, S.; Wu, X.; Chu, W.; Wu, C.; Xie, Y. Controllable Surface Reorganization Engineering on Cobalt Phosphide Nanowire Arrays for Efficient Alkaline Hydrogen Evolution Reaction. *Adv. Mater.* **2018**, *30*, 1703322.

(5) Norskov, J. K.; Christensen, C. H. Toward Efficient Hydrogen Production at Surfaces. *Science* **2006**, *312*, 1322−1323.

(6) Li, W.; Liu, Y.; Wu, M.; Feng, X.; Redfern, S. A. T.; Shang, Y.; Yong, X.; Feng, T.; Wu, K.; Liu, Z.; Li, B.; Chen, Z.; Tse, J. S.; Lu, S.; Yang, B. Carbon-Quantum-Dots-Loaded Ruthenium Nanoparticles as an Efficient Electrocatalyst for Hydrogen Production in Alkaline Media. *Adv. Mater.* **2018**, *30*, 1800676.

(7) Durst, J.; Siebel, A.; Simon, C.; Hasché, F.; Herranz, J.; Gasteiger, H. A. New Insights into the Electrochemical Hydrogen Oxidation and Evolution Reaction Mechanism. *Energy Environ. Sci.* **2014**, *7*, 2255−2260.

(8) Dinh, C.-T.; Jain, A.; de Arquer, F. P. G.; De Luna, P.; Li, J.; Wang, N.; Zheng, X.; Cai, J.; Gregory, B. Z.; Voznyy, O.; Zhang, B.; Liu, M.; Sinton, D.; Crumlin, E. J.; Sargent, E. H. Multi-site Electrocatalysts for Hydrogen Evolution in Neutral Media by Destabilization of Water Molecules. *Nat. Energy* **2019**, *4*, 107−114.

(9) Qin, F.; Zhao, Z.; Alam, M. K.; Ni, Y.; Robles-Hernandez, F.; Yu, L.; Chen, S.; Ren, Z.; Wang, Z.; Bao, J. Trimetallic NiFeMo for Overall Electrochemical Water Splitting with a Low Cell Voltage. *ACS Energy Lett.* **2018**, *3*, 546−554.

(10) McKone, J. R.; Sadtler, B. F.; Werlang, C. A.; Lewis, N. S.; Gray, H. B. Ni-Mo Nanopowders for Efficient Electrochemical Hydrogen Evolution. *ACS Catal.* **2013**, *3*, 166−169.

(11) Su, J.; Yang, Y.; Xia, G.; Chen, J.; Jiang, P.; Chen, Q. Ruthenium-cobalt Nanoalloys Encapsulated in Nitrogen-doped Graphene as Active Electrocatalysts for Producing Hydrogen in Alkaline Media. *Nat. Commun.* **2017**, *8*, 14969.

(12) Luc, W.; Jiang, Z.; Chen, J. G.; Jiao, F. Role of Surface Oxophilicity in Copper-Catalyzed Water Dissociation. *ACS Catal.* **2018**, *8*, 9327−9333.

(13) Staszak-Jirkovsky, J.; Malliakas, C. D.; Lopes, P. P.; Danilovic, N.; Kota, S. S.; Chang, K. C.; Genorio, B.; Strmcnik, D.; Stamenkovic, V. R.; Kanatzidis, M. G.; Markovic, N. M. Design of Active and Stable Co-Mo-Sx Chalcogels as pH-Universal Catalysts for the Hydrogen Evolution Reaction. *Nat. Mater.* **2016**, *15*, 197−203.

(14) Wang, P.; Zhang, X.; Zhang, J.; Wan, S.; Guo, S.; Lu, G.; Yao, J.; Huang, X. Precise Tuning in Platinum-Nickel/Nickel Sulfide Interface Nanowires for Synergistic Hydrogen Evolution Catalysis. *Nat. Commun.* **2017**, *8*, 14580.

(15) Zheng, Y. R.; Wu, P.; Gao, M. R.; Zhang, X. L.; Gao, F. Y.; Ju, H. X.; Wu, R.; Gao, Q.; You, R.; Huang, W. X.; Liu, S. J.; Hu, S. W.; Zhu, J.; Li, Z.; Yu, S. H. Doping-Induced Structural Phase Transition in Cobalt Diselenide Enables Enhanced Hydrogen Evolution Catalysis. *Nat. Commun.* **2018**, *9*, 2533.

(16) Jiang, K.; Liu, B.; Luo, M.; Ning, S.; Peng, M.; Zhao, Y.; Lu, Y. R.; Chan, T. S.; de Groot, F. M. F.; Tan, Y. Single Platinum Atoms Embedded in Nanoporous Cobalt Selenide as Electrocatalyst for Accelerating Hydrogen Evolution Reaction. *Nat. Commun.* **2019**, *10*, 1743.

(17) Shi, Z.; Nie, K.; Shao, Z.-J.; Gao, B.; Lin, H.; Zhang, H.; Liu, B.; Wang, Y.; Zhang, Y.; Sun, X.; Cao, X.-M.; Hu, P.; Gao, Q.; Tang, Y. Phosphorus-Mo_2C@carbon Nanowires toward Efficient Electrochemical Hydrogen Evolution: Composition, Structural and Electronic Regulation. *Energy Environ. Sci.* **2017**, *10*, 1262−1271.

(18) Xu, K.; Sun, Y.; Sun, Y.; Zhang, Y.; Jia, G.; Zhang, Q.; Gu, L.; Li, S.; Li, Y.; Fan, H. J. Yin-Yang Harmony: Metal and Nonmetal Dual-Doping Boosts Electrocatalytic Activity for Alkaline Hydrogen Evolution. *ACS Energy Lett.* **2018**, *3*, 2750−2756.

(19) Tan, Y.; Wang, H.; Liu, P.; Shen, Y.; Cheng, C.; Hirata, A.; Fujita, T.; Tang, Z.; Chen, M. Versatile Nanoporous Bimetallic Phosphides towards Electrochemical Water Splitting. *Energy Environ. Sci.* **2016**, *9*, 2257−2261.

(20) Chen, G.; Wang, T.; Zhang, J.; Liu, P.; Sun, H.; Zhuang, X.; Chen, M.; Feng, X. Accelerated Hydrogen Evolution Kinetics on NiFe-Layered Double Hydroxide Electrocatalysts by Tailoring Water Dissociation Active Sites. *Adv. Mater.* **2018**, *30*, 1706279.

(21) Zhang, C.; Liu, Y.; Chang, Y.; Lu, Y.; Zhao, S.; Xu, D.; Dai, Z.; Han, M.; Bao, J. Component-Controlled Synthesis of Necklace-Like Hollow Ni_XRu_y Nanoalloys as Electrocatalysts for Hydrogen Evolution Reaction. *ACS Appl. Mater. Interfaces* **2017**, *9*, 17326−17336.

(22) Lu, Q.; Hutchings, G. S.; Yu, W.; Zhou, Y.; Forest, R. V.; Tao, R.; Rosen, J.; Yonemoto, B. T.; Cao, Z.; Zheng, H.; Xiao, J. Q.; Jiao, F.; Chen, J. G. Highly Porous Non-Precious Bimetallic Electrocatalysts for Efficient Hydrogen Evolution. *Nat. Commun.* **2015**, *6*, 6567.

(23) Zhang, P.; Wang, M.; Chen, H.; Liang, Y.; Sun, J.; Sun, L. A Cu-Based Nanoparticulate Film as Super-Active and Robust Catalyst Surpasses Pt for Electrochemical H_2Production from Neutral and Weak Acidic Aqueous Solutions. *Adv. Energy Mater.* **2016**, *6*, 1502319.

(24) Mao, J.; He, C. T.; Pei, J.; Chen, W.; He, D.; He, Y.; Zhuang, Z.; Chen, C.; Peng, Q.; Wang, D.; Li, Y. Accelerating Water Dissociation Kinetics by Isolating Cobalt Atoms into Ruthenium Lattice. *Nat. Commun.* **2018**, *9*, 4958.

(25) Lu, B.; Guo, L.; Wu, F.; Peng, Y.; Lu, J. E.; Smart, T. J.; Wang, N.; Finfrock, Y. Z.; Morris, D.; Zhang, P.; Li, N.; Gao, P.; Ping, Y.; Chen, S. Ruthenium Atomically Dispersed in Carbon Outperforms Platinum toward Hydrogen Evolution in Alkaline Media. *Nat. Commun.* **2019**, *10*, 631.

(26) Zheng, Y.; Jiao, Y.; Zhu, Y.; Li, L. H.; Han, Y.; Chen, Y.; Jaroniec, M.; Qiao, S. Z. High Electrocatalytic Hydrogen Evolution Activity of an Anomalous Ruthenium Catalyst. *J. Am. Chem. Soc.* **2016**, *138*, 16174−16181.

(27) Zhang, J.; Liu, P.; Wang, G.; Zhang, P. P.; Zhuang, X. D.; Chen, M. W.; Weidinger, I. M.; Feng, X. L. Ruthenium/Nitrogen-Doped Carbon as an Electrocatalyst for Efficient Hydrogen Evolution in Alkaline Solution. *J. Mater. Chem. A* **2017**, *5*, 25314−25318.

(28) Mahmood, J.; Li, F.; Jung, S. M.; Okyay, M. S.; Ahmad, I.; Kim, S. J.; Park, N.; Jeong, H. Y.; Baek, J. B. An Efficient and pH-Universal Ruthenium-Based Catalyst for the Hydrogen Evolution Reaction. *Nat. Nanotechnol.* **2017**, *12*, 441−446.

(29) Xu, J.; Liu, T.; Li, J.; Li, B.; Liu, Y.; Zhang, B.; Xiong, D.; Amorim, I.; Li, W.; Liu, L. Boosting the Hydrogen Evolution Performance of Ruthenium Clusters through Synergistic Coupling with Cobalt Phosphide. *Energy Environ. Sci.* **2018**, *11*, 1819−1827.

(30) Lu, Q.; Wang, A. L.; Gong, Y.; Hao, W.; Cheng, H.; Chen, J.; Li, B.; Yang, N.; Niu, W.; Wang, J.; Yu, Y.; Zhang, X.; Chen, Y.; Fan, Z.; Wu, X. J.; Chen, J.; Luo, J.; Li, S.; Gu, L.; Zhang, H. Crystal Phase-based Epitaxial Growth of Hybrid Noble Metal Nanostructures on 4H/fcc Au Nanowires. *Nat. Chem.* **2018**, *10*, 456−461.

(31) Erlebacher, J.; Aziz, M. J.; Karma, A.; Dimitrov, N.; Sieradzki, K. Evolution of Nanoporosity in Dealloying. *Nature* **2001**, *410*, 450−453.

(32) Qiu, H.-J.; Kang, J. L.; Liu, P.; Hirata, A.; Fujita, T.; Chen, M. W. Fabrication of Large-scale Nanoporous Nickel with a Tunable Pore Size for Energy Storage. *J. Power Sources* **2014**, *247*, 896−905.

(33) Luc, W.; Jiao, F. Nanoporous Metals as Electrocatalysts: State-of-the-Art, Opportunities, and Challenges. *ACS Catal.* **2017**, *7*, 5856−5861.

(34) Luc, W.; Jiao, F. Synthesis of Nanoporous Metals, Oxides, Carbides, and Sulfides: Beyond Nanocasting. *Acc. Chem. Res.* **2016**, *49*, 1351−8.

(35) Fujita, T.; Guan, P. F.; McKenna, K.; Lang, X. Y.; Hirata, A.; Zhang, L.; Tokunaga, T.; Arai, S.; Yamamoto, Y.; Tanaka, N.; Ishikawa, Y.; Asao, N.; Yamamoto, Y.; Erlebacher, J.; Chen, M. W.

DOI: 10.1021/acsenergylett.9b02374
ACS Energy Lett. 2020, 5, 192−199

Atomic Origins of the High Catalytic Activity of Nanoporous Gold. *Nat. Mater.* **2012**, *11*, 775−780.
(36) Wang, F. L.; Kusada, K.; Wu, D. S.; Yamamoto, T.; Toriyama, T.; Matsumura, S.; Nanba, Y.; Koyama, M.; Kitagawa, H. Solid-Solution Alloy Nanoparticles of the Immiscible Iridium-Copper System with a Wide Composition Range for Enhanced Electrocatalytic Applications. *Angew. Chem., Int. Ed.* **2018**, *57*, 4505−4509.
(37) Huang, B.; Kobayashi, H.; Yamamoto, T.; Matsumura, S.; Nishida, Y.; Sato, K.; Nagaoka, K.; Kawaguchi, S.; Kubota, Y.; Kitagawa, H. Solid-Solution Alloying of Immiscible Ru and Cu with Enhanced CO Oxidation Activity. *J. Am. Chem. Soc.* **2017**, *139*, 4643−4646.
(38) Chen, C. H.; Wu, D.; Li, Z.; Zhang, R.; Kuai, C. G.; Zhao, X. R.; Dong, C. K.; Qiao, S. Z.; Liu, H.; Du, X. W. Ruthenium-Based Single-Atom Alloy with High Electrocatalytic Activity for Hydrogen Evolution. *Adv. Energy Mater.* **2019**, *9*, 1803913.
(39) Li, F.; Han, G.-F.; Noh, H.-J.; Ahmad, I.; Jeon, I.-Y.; Baek, J.-B. Mechanochemically Assisted Synthesis of a Ru Catalyst for Hydrogen Evolution with Performance Superior to Pt in Both Acidic and Alkaline Media. *Adv. Mater.* **2018**, *30*, 1803676.
(40) Liu, Y.; Liu, S.; Wang, Y.; Zhang, Q.; Gu, L.; Zhao, S.; Xu, D.; Li, Y.; Bao, J.; Dai, Z. Ru Modulation Effects in the Synthesis of Unique Rod-like Ni@Ni_2P-Ru Heterostructures and Their Remarkable Electrocatalytic Hydrogen Evolution Performance. *J. Am. Chem. Soc.* **2018**, *140*, 2731−2734.
(41) Panda, C.; Menezes, P. W.; Zheng, M.; Orthmann, S.; Driess, M. In Situ Formation of Nanostructured Core-Shell Cu_3N-CuO to Promote Alkaline Water Electrolysis. *ACS Energy Lett.* **2019**, *4*, 747−754.
(42) Zhang, J.; Wang, T.; Liu, P.; Liu, S.; Dong, R.; Zhuang, X.; Chen, M.; Feng, X. Engineering Water Dissociation Sites in MoS_2 Nanosheets for Accelerated Electrocatalytic Hydrogen Production. *Energy Environ. Sci.* **2016**, *9*, 2789−2793.
(43) Ye, R.; Liu, Y.; Peng, Z.; Wang, T.; Jalilov, A. S.; Yakobson, B. I.; Wei, S. H.; Tour, J. M. High Performance Electrocatalytic Reaction of Hydrogen and Oxygen on Ruthenium Nanoclusters. *ACS Appl. Mater. Interfaces* **2017**, *9*, 3785−3791.
(44) Zhu, Y.; Tahini, H. A.; Hu, Z.; Dai, J.; Chen, Y.; Sun, H.; Zhou, W.; Liu, M.; Smith, S. C.; Wang, H.; Shao, Z. Unusual Synergistic Effect in Layered Ruddlesden-Popper Oxide Enables Ultrafast Hydrogen Evolution. *Nat. Commun.* **2019**, *10*, 149.
(45) Laursen, A. B.; Patraju, K. R.; Whitaker, M. J.; Retuerto, M.; Sarkar, T.; Yao, N.; Ramanujachary, K. V.; Greenblatt, M.; Dismukes, G. C. Nanocrystalline Ni_5P_4: A Hydrogen evolution Electrocatalyst of Exceptional Efficiency in both Alkaline and Acidic Media. *Energy Environ. Sci.* **2015**, *8*, 1027−1034.
(46) Yang, F.; Zhao, Y.; Du, Y.; Chen, Y.; Cheng, G.; Chen, S.; Luo, W. A Monodisperse Rh_2P-Based Electrocatalyst for Highly Efficient and pH-Universal Hydrogen Evolution Reaction. *Adv. Energy Mater.* **2018**, *8*, 1703489.
(47) Xing, Z.; Han, C.; Wang, D.; Li, Q.; Yang, X. Ultrafine Pt Nanoparticle-Decorated $Co(OH)_2$ Nanosheet Arrays with Enhanced Catalytic Activity toward Hydrogen Evolution. *ACS Catal.* **2017**, *7*, 7131−7135.
(48) Peng, Z.; Jia, D.; Al-Enizi, A. M.; Elzatahry, A. A.; Zheng, G. From Water Oxidation to Reduction: Homologous Ni-Co Based Nanowires as Complementary Water Splitting Electrocatalysts. *Adv. Energy Mater.* **2015**, *5*, 1402031.
(49) Cao, L.; Luo, Q.; Liu, W.; Lin, Y.; Liu, X.; Cao, Y.; Zhang, W.; Wu, Y.; Yang, J.; Yao, T.; Wei, S. Identification of Single-atom Active Sites in Carbon-based Cobalt Catalysts during Electrocatalytic Hydrogen Evolution. *Nat. Catal.* **2019**, *2*, 134−141.
(50) Luo, M.; Guo, S. Strain-controlled Electrocatalysis on Multimetallic Nanomaterials. *Nat. Rev. Mater.* **2017**, *2*, 17059.

■ NOTE ADDED AFTER ASAP PUBLICATION

This article published December 13, 2019 with typos in Figure 1. The corrected figure published December 17, 2019.

DOI: 10.1021/acsenergylett.9b02374
ACS Energy Lett. 2020, 5, 192−199